

FEMTOSECOND DYNAMICS OF ELECTRONS ON SURFACES AND AT INTERFACES¹

*C. B. Harris, N.-H. Ge, R. L. Lingle, Jr.², J. D. McNeill,
and C. M. Wong*

Department of Chemistry, University of California, Berkeley, California 94720, and
Chemical Sciences Division, E. O. Lawrence Berkeley National Laboratory, Berkeley,
California 94720

KEY WORDS: carrier dynamics, metal-dielectric interfaces, two-photon photoemission,
interfacial quantum wells, localization, small polarons

ABSTRACT

Two-photon photoemission is a promising new technique that has been developed for the study of electron dynamics at interfaces. A femtosecond laser is used to both create an excited electronic distribution at the surface and eject the distribution for subsequent energy analysis. Time- and momentum-resolved two-photon photoemission spectra as a function of layer thickness fully determine the conduction band dynamics at the interface. Earlier clean surface studies showed how excited electron lifetimes are affected by the crystal band structure and vacuum image potential. Recent studies of various insulator/metal interfaces show that the dynamics of excess electrons are largely determined by the electron affinity of the adsorbate. In general, electron dynamics at the interface are influenced by the substrate and adlayer band structures, dielectric screening, and polaron formation in the two-dimensional overlayer lattice.

INTRODUCTION

The energy levels, transport properties, and dynamics of excited electrons at surfaces and interfaces are important in surface chemistry, electrochemistry, electronic materials, and the optical properties of interfaces. For example, hot

¹The US Government has the right to retain a nonexclusive royalty-free license in and to any copyright covering this paper.

²Permanent address: Lucent Technologies, Bell Laboratories, Suite G010, 2000 NE Expressway, Norcross, Georgia 30071.

photoexcited electrons at surfaces can induce electronic transition to dissociative states, thereby causing fragmentation and/or desorption of adsorbates (1). Electron dynamics at metal-semiconductor (2) and metal-metal interfaces (3) have been reviewed recently. This review focuses on progress made in the past few years toward understanding electron dynamics at nanometer metal-insulator interfaces. In addition to fundamental questions regarding the transition from two-dimensional (2-D) to 3-D electronic structure and nanoscale physics, there are many applications involving the interaction of charges with metal-insulator interfaces: dielectrics in microelectronic circuits, spacer layers in photochemical studies, screening effects in ion desorption and electron spectroscopies, and electronic structure at metal-organic device junctions.

Theoretical studies on surface states were pioneered by Tamm (4), Maue (5), Goodwin (6, 7), and Shockley (8). Most surface states arise from the loss of periodicity of the bulk, which results in states that are localized in the vicinity of the surface of a crystal (9). These surface states or surface bands typically reside in a bulk band gap. Surface resonances occur in the case of degeneracy with bulk bands. The wave function that describes a surface state can often be factored into components parallel and perpendicular to the interface. The parallel wave function is a free-electron-like plane or Bloch wave, while the perpendicular wave function has its maximum amplitude in the surface region, representing most of the physics unique to the interface. One class of surface states, however, arises from the abrupt change of polarizability at an interface rather than from the loss of periodicity. For a bare metal, an electron in the vacuum is attracted to the polarization it induces in the surface. This problem is often solved in elementary electrostatics by the method of images (10, 11), in which the electron at a distance z from a surface interacts with a fictitious image charge located at $-z$. This simple charge configuration mimics the boundary conditions for an electric field in the presence of a perfect conductor and thus provides the unique solution to Poisson's equation: a 1-D $1/4z$ Coulomb potential. For the idealized case of a completely reflective metal surface, the image potential results in the formation of a Rydberg series of image potential states converging to the vacuum level (Figure 1). The wave function of an image state electron can be approximated by z times the radial part of the hydrogenic wave function scaled for the factor of $1/4$. The image potential for nonmetallic surfaces is $\frac{-(\epsilon-1)}{4(\epsilon+1)z}$.

Image potential states were first observed on the surface of liquid helium, where transitions were detected by microwave absorption (12). The first evidence for image potential states on bare metals was obtained by inverse photoemission (13–15). Steinmann, Himpfel, and coworkers first studied this class of surface states by two-photon photoemission (TPPE) with nanosecond lasers (16). This and subsequent TPPE work led to confirmation of the multiple reflection theory for image state binding energies on different single-crystal

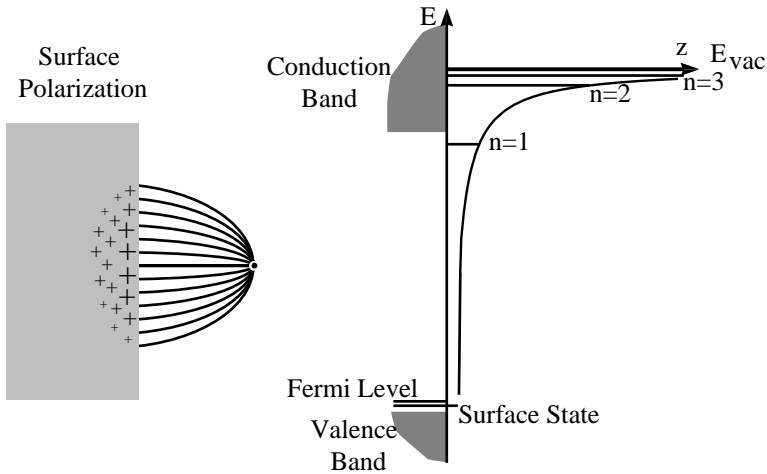


Figure 1 An electron near a surface is bound by an image potential that the electron induces by polarizing the material. Image states form a Rydberg series of states that converge to the vacuum level. The Ag(111) band structure is shown here for zero momentum parallel to the surface. The lifetimes for $n = 2, 3$ are anomalously short on Ag(111) as a result of degeneracy with the conduction band.

metal faces. In recent years, however, the studies of image states in the presence of overlayers provided a new tool for characterizing and studying many important properties of interfaces on the nanometer scale.

Image Potential Electrons as Probes of Dynamics at Interfaces

The simple Coulomb interaction of an excess electron with a surface can be altered significantly by any factor which changes the dielectric susceptibility at the interface. Therefore electrons in image potential states can serve as sensitive probes of layer-by-layer changes in electronic structure and dynamics. Steinmann, Fauster, and coworkers used the fact that image state binding energies are pinned to the local work function (17) to observe the growth modes of Ag, Au, and Co on Cu(111) and Pd(111) (18–20) and have studied the evolution of metallic quantum wells for Au/Pd(111) (19). These studies examine the formation of an ultrathin interface of one free-electron material on another and were recently reviewed (3). Harris and coworkers have shown that the modification of image potential states by the presence of dielectric overlayers can be used to study electronic structure and dynamics at interfaces in layer-by-layer fashion (21).

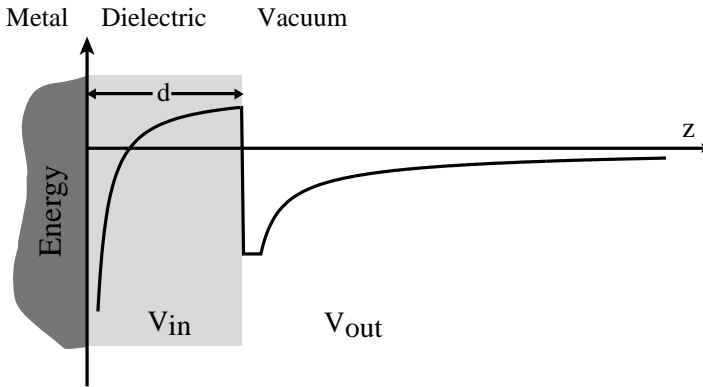


Figure 2 The potential described by the dielectric continuum model, where d is the layer thickness. See Equations 1 and 2.

Before reviewing what has been learned about ultrathin interfaces by studying the evolution of image states, it is instructive to ask what are the simplest possible effects due to a dielectric overlayer on a metal surface. The simplest model is that of a continuum dielectric layer on a perfect conductor in vacuum (22), as illustrated in Figure 2. The simple image potential picture is modified in two major physical ways. First the electron polarizes the dielectric slab; this is an attractive interaction tending to increase the electron's binding energy. However, the polarization of the dielectric slab also serves to screen the image electric field between the metal and the electron, tending to reduce the binding of the electron to the metal. The net effect could then be to either increase or decrease the binding energy relative to that of the bare metal.

This electrostatic problem of a charge outside a perfect metal with a continuum dielectric overlayer can be solved as a first attempt at modeling these effects. An example of the resulting potential is shown in Figure 2:

$$V_{\text{in}}(z) = V_0 - \frac{e^2}{4\epsilon z}, \quad 1.$$

$$V_{\text{out}}(z, d) = \frac{-\beta e^2}{4(z-d)} + \frac{(1-\beta^2)e^2}{4\beta} \sum_{n=1}^{\infty} \frac{(-\beta)^n}{z-d+nd}, \quad 2.$$

where z is the distance from the metal, d is the layer thickness, ϵ is the

static dielectric constant of the adlayer, V_0 is the adlayer electron affinity, and $\beta = (\epsilon - 1)/(\epsilon + 1)$. Inside the dielectric, the image potential of the metal is screened by the presence of the dielectric layer, as shown by the factor of ϵ^{-1} in Equation 1. The potential outside is due to the response of the polarizable composite interface to the presence of the excess charge; the potential explicitly depends on the dielectric constant and the layer thickness. A potential of this basic form was used by Cole (22) in 1971 to describe a hypothetical liquid helium/metal interface, while Lingle et al (23) and McNeill et al (24) have used variations of the potential of Equations 1 and 2 to describe metal-dielectric interfaces as discussed in this review. These dielectric screening effects should be relevant for any dielectric overlayer and will be important for a quantitative understanding of electron binding energies at the interface.

Recently, however, it has been learned that the electron affinity of the overlayer material plays perhaps the most dramatic role in determining the electronic structure and dynamics of electrons at ultrathin dielectric-on-metal interfaces. The electron affinity appears as an additive constant in Equation 1, raising or lowering the electrostatic potential inside the adlayer to take some account of the fact that the overlayer has a band structure. We demonstrate below that a positive (attractive) affinity overlayer leads to quantum well states (24–26), whereas a negative (repulsive) affinity overlayer represents a tunneling barrier that dominates the energies and lifetimes (23). The results of studying representative cases of these two classes are reviewed in detail here, with general implications for predicting electronic structure and dynamics at interfaces.

Furthermore, it has been learned that electrons in some ultrathin overlayers undergo rapid self-trapping on the 10^{-13} s time scale (25, 27), while conduction electrons remain extended for other cases (24). The data suggest that an initially delocalized electron at the interface forms a polaron, i.e. a carrier accompanied by a lattice deformation. The detailed information on electron dynamics and effective masses in these molecular overlayers enables a theoretical treatment that may yield quantitative information on the electron-medium interaction energy and the lattice vibrational mode that mediates polaron formation. There is an intriguing analogy between trends for electron trapping at interfaces and those for mobility of electrons in thermal equilibrium in bulk fluids.

The cases discussed in this review involve atoms and molecules that do not chemically bond to the surface and have no low-lying molecular electronic states energetically close to the image potential states. The adlayer states near the vacuum level exist because the high-lying atomic orbitals overlap to form a band. The bottom of this conduction band may be above or below the vacuum level and defines the electron affinity. On the other hand, even an isolated benzene molecule on a metal surface has a stable anion (28) as a result of image

stabilization. Early study of systems of this type showed complex spectra that are not yet understood (21).

Time and Angle-Resolved Two-Photon Photoemission Spectroscopy

Unoccupied electronic structure and dynamics at interfaces can be studied by time- and angle-resolved TPPE. Angle-resolved photoemission is a well-established technique useful for determining band gaps and valence (occupied) band structure (29). In general, photoemission requires the use of a photon whose energy is greater than the substrate work function, ejecting an electron from an occupied level below the Fermi energy. In TPPE, one photon excites the electron from an occupied bulk or crystal-induced surface state into an unoccupied state (the state of interest) between the vacuum and Fermi levels; a second photon photoejects the electron into the vacuum for detection. TPPE thus differs from ordinary photoemission in that the kinetic energy of the photoemitted electron is determined by the photon energy and the binding energy of the intermediate state, rather than the initial state. Other techniques for probing the unoccupied band structure and surface state electronic structure, such as inverse photoemission and scanned tunneling spectroscopy, currently lack sufficient energy, momentum, or time resolution. TPPE has been described in detail in several places (2, 3, 21) and is described briefly below.

Using two-color TPPE, it is possible to reduce the energy background and eliminate space charge broadening by reducing the intensity of the pump pulse and increasing the intensity of the probe pulse to get higher electron count rates. Time-of-flight single-electron counting yields the best energy resolution and signal-to-noise and reduces space charge broadening. Harris and coworkers first used high-repetition rate picosecond (then femtosecond) lasers with repetition rates of 2 MHz (then 200 kHz) (21, 23). One electron is detected per 20 laser pulses, so space charge is practically eliminated and high kHz electron count rates are maintained. A schematic setup of a TPPE experiment is shown in Figure 3. The two-color UV pump, visible probe experiment permits detection of the image state photoelectrons in the 1-eV kinetic energy range. Features as narrow as 20 meV have been observed for a monolayer of Xe/Ag(111) (30).

For a well-ordered surface, the momentum component parallel to the surface (k_{\parallel}) is conserved in the photoemission process. Thus the parallel dispersion $E(k_{\parallel})$ of surface or bulk band structure can be mapped out by varying the angle of the sample with respect to the detector. The k_{\parallel} component of the emitting state can then be determined as

$$k_{\parallel} = \sin \theta \frac{\sqrt{2m_e E_{\text{kin}}}}{\hbar}, \quad 3.$$

where θ is the angle of the surface normal with respect to the detector, m_e is the

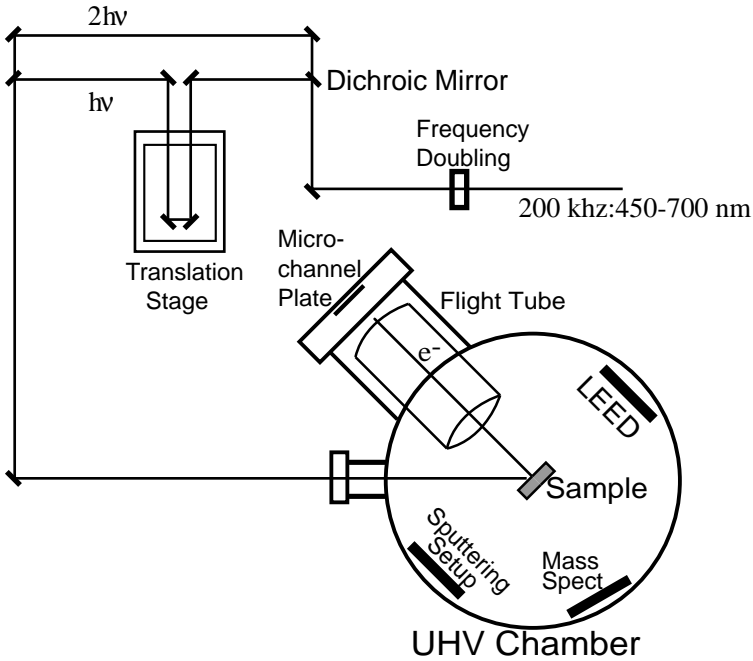


Figure 3 Schematic of a two-color TPPE experimental apparatus with a tunable femtosecond laser.

electron mass of the photoemitted electron, and E_{kin} is the measured electron kinetic energy. The energy of the emitting state in the direction parallel to the surface is then given as

$$E_i = E_0 + \frac{\hbar^2 k_{\parallel}^2}{2m^*}, \tag{4}$$

where E_0 is the energy of the emitting state at $k_{\parallel} = 0$, and m^* is the effective mass.

The effective mass can be determined by the curvature of an E_i versus k_{\parallel} plot and is a measure of the coupling of the electron with the bulk or an overlayer. For example, the effective mass for the clean surface Ag(111) $n = 1$ image state is about $1.3m_e$ (30, 31), as determined by two photon photoemission, which is somewhat heavier than the mass of a free electron as a result of the influence of the relatively flat Ag(111) surface-projected conduction band.

Direct measurement of electron dynamics can be obtained by varying the delay between the pump and probe pulses. Fujimoto and coworkers (32–34)

were the first to make these measurements for clean metal surfaces; they studied $n = 1, 2$ image potential lifetimes on Ag(111) and Ag(100). These studies confirmed the prediction that image state lifetimes vary as n^3 (35). Harris and coworkers have studied dielectric overlayers on metal substrates with 70-fs pulses (23). Ertl and coworkers have observed that linewidths demand that image potential electron time-dependence be interpreted as coherent dynamics (36). Fauster and coworkers have recently taken advantage of this slow dephasing to observe coherent oscillations between emission from the higher quantum states on Ag(100) (37).

Surface Physics of the Image Potential and Metal Substrate

Although this paper discusses the quantum mechanical bound states supported by the image potential, the image potential itself appears in numerous contexts in physical chemistry. For example, the screened image potential plays a role in forming the field-dependent barrier for charge injection from a metal into a semiconductor or organic semiconductor (38). The image potential also plays an important role in understanding common interface processes such as photoemission and the desorption of ions (39–43). Quantitative models of these effects on metals have frequently incorporated the displaced image potential model first used by Gomer & Swanson: $V_I(z) = -e^2/4(z + \kappa^{-1})$ (44). The introduction of the Thomas-Fermi screening parameter κ allows the potential to vary weakly with the free electron density n_0 of the metal, since κ is directly proportional to $n_0^{1/6}$. However, calculations of image electron binding energies usually neglect the dependence on n_0 and concentrate on the effect due to the band structure of the metal substrate.

The projected bulk band structure of Ag(111) is shown in Figure 4. The gap along the surface normal, which extends from the top of the valence band at 300 meV below the Fermi energy to 500 meV below the vacuum level, determines the binding energies of surface electronic states (3, 45). Briefly, the wave functions for states near the top or bottom of the gap will penetrate deeper into the metal and be short lived, while states near the center of the gap in the projected band structure have less probability density in the substrate and will be longer lived. Since image potential Rydberg states converge to the vacuum level, a necessary condition for the existence of energetically narrow, true surface states (as opposed to broad resonances) is that the vacuum level be below or only slightly above the top of the gap.

A useful physical picture relating the metal band structure and the image potential to the image electron eigenenergies on bare metal surfaces emerges from the multiple reflection theory (MRT) or phase-shift analysis. The image potential state is represented as a plane wave that propagates between the reflecting barrier of the metal crystal band gap and the image potential in the vacuum.

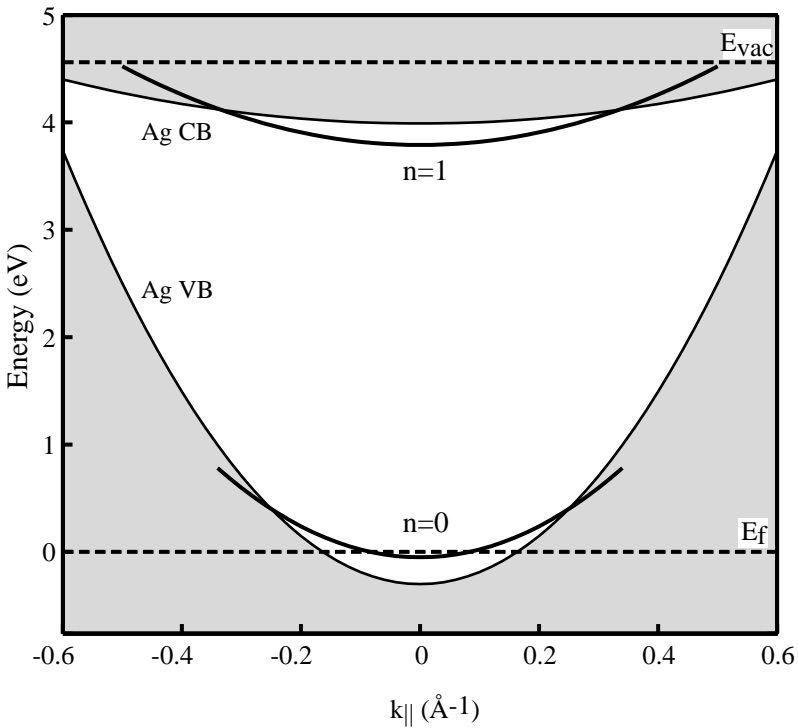


Figure 4 Surface projected bulk band structure for Ag(111). The $n = 0$ and $n = 1$ surface states are also displayed.

Bound states occur when the total accumulated phase is an integral multiple of 2π . The MRT formalism is simply a way to solve the matching condition between the substrate wave function and the hydrogenic wave function in the vacuum. Reviews on applications of MRT have been written by Smith (46) and also by Echenique & Pendry (45).

For the Coulomb potential in the vacuum, the boundary conditions require the solution to the time-independent Schrödinger equation to vanish at infinity; thus the solution is a confluent hypergeometric function called the irregular Whittaker function (47). The wave function inside a metal can be approximated using the two-band nearly free electron (NFE) model. The main features described by the two-band NFE model are two bands and an energy gap, which are the primary features defining the projected bulk band structure in Figure 4. Image states generally exist within this gap where electrons impinging on the metal surface are Bragg reflected.

In NFE, the crystal potential of the ion core can be expanded in a Fourier series leading to the following secular equation

$$\begin{vmatrix} (\hbar^2/2m^*)k^2 - \varepsilon & V_g \\ V_g & (\hbar^2/2m^*)(k - g)^2 - \varepsilon \end{vmatrix} = 0, \quad 5.$$

where V_g is the gap half-width, ε is the energy of the electron, and m^* is the effective mass along the surface normal. Within the gap, the wave vector k is a complex quantity with the real and imaginary parts equal to p and q , respectively. The imaginary part q causes the wave to decay exponentially into the metal, and Equation 5 yields

$$p = g/2, \quad 6.$$

$$(\hbar^2/2m^*)q^2 = (4\varepsilon E_g + V_g^2)^{1/2} - (\varepsilon + E_g), \quad 7.$$

$$E_g = (\hbar^2/2m^*)p^2, \quad 8.$$

$$\sin(2\delta) = -(\hbar^2/2m^*)(pq/V_g), \quad 9.$$

where E_g is the midgap energy, a is the interplanar spacing, and $g = 2\pi/a$. The wave function in the crystal is then given as

$$\psi_B = e^{qz} \cos(pz + \delta). \quad 10.$$

DIELECTRIC EFFECTS AT MONOLAYER INSULATOR/METAL INTERFACES

Early work by Steinmann and coworkers showed that the image potential state photoelectron signal was quenched by the presence of $O_2/Ag(100)$ (48). This was attributed to a significant decrease in image potential state lifetime due to scattering from molecular oxygen. However, Harris and coworkers (21, 30) found that image potential states persist in the presence of physisorbed rare gas and alkane overlayers. In fact, narrow and well-separated peaks due to different image potential state quantum number and overlayer thickness were observed. This observation demonstrated the feasibility of using the binding energies, effective masses, and lifetimes of image potential electrons as sensitive probes of electron behavior at nanometer interfaces.

The body of this review begins with a summary of results for dielectric monolayers on metal surfaces. The $n = 1$ image potential binding energies for rare gases and alkanes on $Ag(111)$ were extensively investigated (21, 30, 49). It was at first surprising that most overlayers studied—including xenon, cyclohexane, n-hexane, n-heptane, and n-octane—all had binding energies in the range of -690 to -660 meV. Upon Xe adsorption, the $Ag(111)$ $n = 1$ image potential

linewidth narrowed from 40 to 25 meV, which was attributed to a longer lifetime in the presence of the monolayer. Most of the binding energy shift could be accounted for within MRT by noting that the work function change due to physisorption (450 to 500 meV) causes the vacuum level to shift with respect to the Fermi level, changing the energetic relationship of the image states with respect to the band structure of the metal. The result is that most of the binding energy shift for monolayers is due to the work function change. The question arises, how important are dielectric effects in the monolayer limit?

This question can be answered by considering again the model potential shown in Figure 2 and Equations 1 and 2. This potential quantifies the two previously described dielectric effects: The presence of a dielectric layer weakens the interaction between an exterior charge and the metal but adds a new attraction between the charge and the adlayer itself. Dielectric screening of the electron-metal interaction is contained in the second terms of both Equations 1 and 2, which decrease as ϵ increases. The attractive interaction between the excess charge and the dielectric overlayer is represented by the first term in Equation 2, which becomes more prominent as ϵ increases. Eigenvalue calculations of image state binding energies using a potential of this form indicate that the binding energies for metal-dielectric layers are the net result of these competing interactions. As shown in Figure 5, dielectric screening dominates for lower values of dielectric constant, leading to lower values of binding energy than for the bare surface. Higher values of dielectric constant eventually lead to stronger binding than for the bare surface.

The qualitative predictions of Figure 5 have been confirmed by studying a series of n-alkanes/Ag(111) from methane to n-decane (49). The purpose of comparing the binding energies of n-alkanes is to vary the dielectric parameter while holding other factors constant, such as adlayer thickness. Figure 6 shows that monolayer $n = 1$ binding energies do increase with n-alkane chain length, and thus dielectric constant. From this model, we conclude that dielectric effects are indeed significant for the monolayer but that values around $\epsilon = 2$ are in the range where the competing dielectric effects are roughly in balance. It is interesting to note that the correlation between binding energy and the molecular polarizability α is rather linear and suggests that monolayer properties might be better modeled based on a molecular parameter than the bulk parameter ϵ .

DIELECTRIC OVERLAYERS WITH REPULSIVE ELECTRON AFFINITY

Beyond the monolayer, the electron affinity of the overlayer slab becomes important while dielectric effects persist. The combined results of these effects is a very sensitive dependence on layer thickness and susceptibility (parameterized

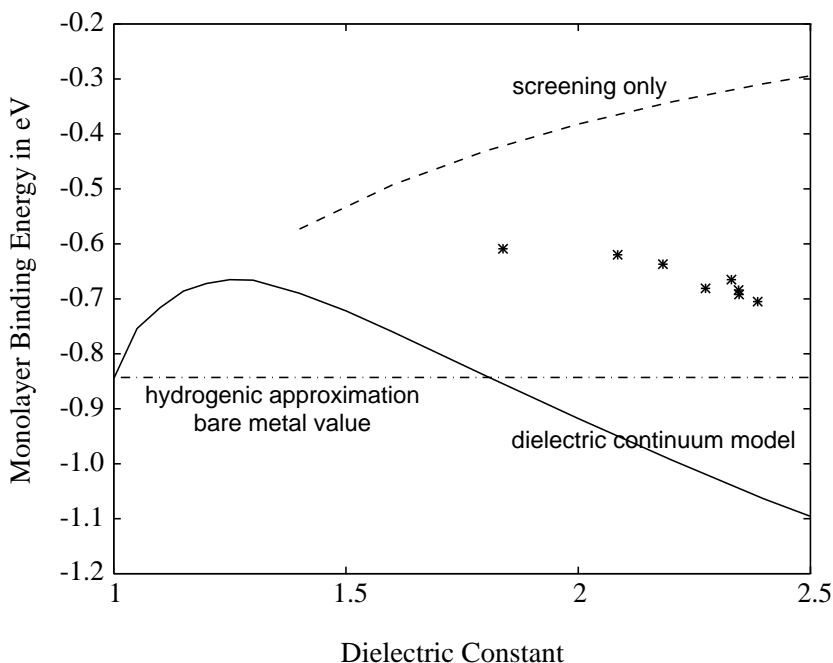


Figure 5 Calculated binding energy as a function of dielectric constant within the dielectric continuum model (*solid line*). The dashed line shows the result for artificially eliminating the attractive interaction with the dielectric layer from the potential of Equations 1 and 2, thus considering only the screening effect. Experimental results for a series of n-alkanes are represented by *; the point with lowest estimated dielectric constant is for methane and the highest is for n-decane. No attempt was made here to fit the model results to the data. However, the tendency for binding energy to increase (become more negative) as dielectric constant increases is reproduced for a wide range of model parameters.

by α or ϵ). For example, Figure 7 illustrates how well-separated are the peaks for pentane or neopentane up to three layers (50). This illustrates that layer growth can, in many cases, be monitored in situ in the TPPE spectrum. The neopentane monolayer exhibits a bigger shift in binding energy than n-pentane due to more efficient screening, since the neopentane layer is thicker. However, by the trilayer n-pentane has the lowest binding energy, owing to the fact that n-pentane has a repulsive affinity and neopentane has an attractive affinity. Although this review focuses on the behavior of electrons at interfaces, we note here that the behavior of electrons, once understood, can be used to study

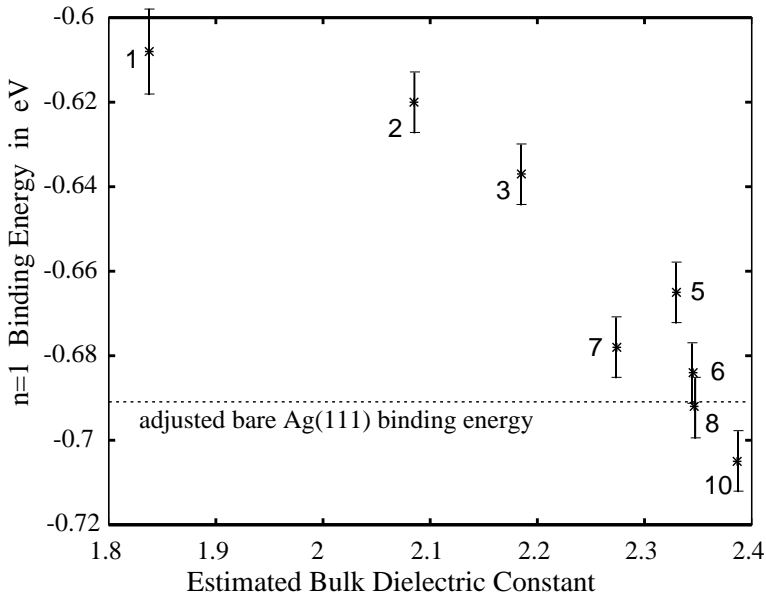


Figure 6 Experimental binding energies for the $n = 1$ state in the presence of a monolayer of n -alkanes, from Reference (49). The chain length is indicated in the graph.

adsorption, layer growth morphology, and phase transitions. For example, the fact that the monolayer spectrum of n -pentane in Figure 7 shows a well-defined nascent bilayer peak means that bilayer islands, rather than isolated and scattered molecules, are forming on the completed monolayer. Island formation down to a few percent of a monolayer can be observed by TPPE.

The dielectric continuum picture is expected to be quantitatively more meaningful beyond the monolayer. Indeed, Harris and coworkers (23) have shown that multilayer binding energies for up to ten layers of n -octane can be successfully modeled by parameters that are reasonably close to those of bulk n -octane. However, the use of estimated bulk parameters and the unrealistic treatment of the adlayer-vacuum interface prevent this model from being totally satisfactory for quantitative predictions. The model does, however, capture the essential physics.

The 1-D model potential of Equations 1 and 2 indicates that the tunneling barrier shown in Figure 8 tends to exclude the electrons from the overlayer region, where they behave as image states of the composite metal-dielectric interface.

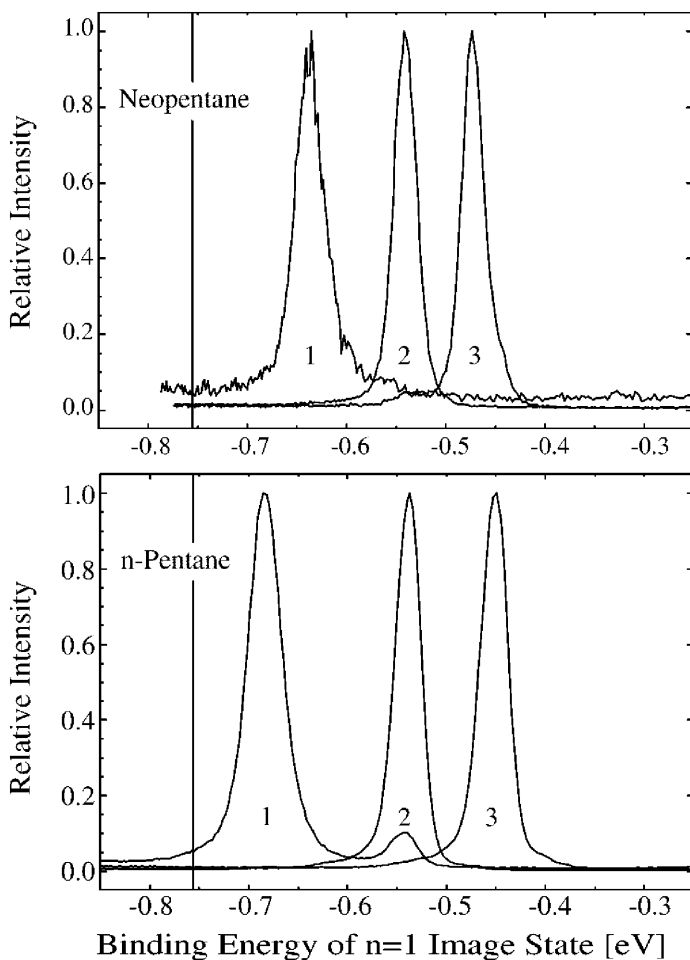


Figure 7 Spectra for the $n = 1$ image state showing its change in binding energy as a function of layer thickness for neopentane and n-pentane. Numbers indicate number of layers, and vertical lines indicate clean surface $n = 1$ binding energy. [Adapted from Reference (50).]

According to this picture, dramatic lengthening of the lifetimes should occur with increasing layer thickness. In fact, Cole (22) considered this question using the potential shown in Figure 8 and modeled two effects: the probability of tunneling through the barrier, and the classical oscillation time in the outer well (vacuum image potential). The tunneling probability depends on the barrier width and height, both of which become larger for more negative eigenenergies.

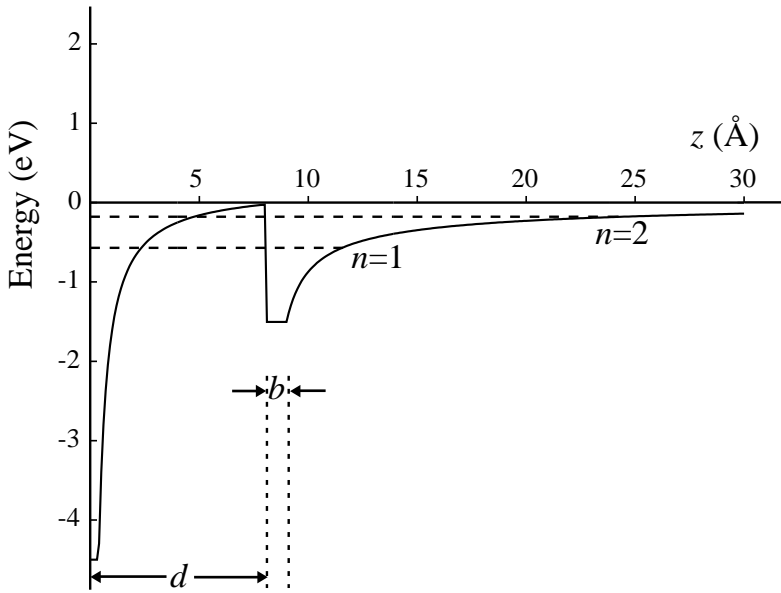


Figure 8 Dielectric continuum model for a bilayer of n-heptane, where d is the layer thickness. A potential cutoff is imposed for a length of b to avoid the singularity in the potential.

This means that we expect the lower quantum states to have longer lifetimes due to tunneling. On the other hand, the classical oscillation time in the outer well will become longer for binding energies closer to the vacuum level. A less bound image electron will experience a flatter part of the Coulomb potential and a concomitantly softer restoring force, thus spending more time at the outer turning point and less time near the metal where it could couple to the bulk conduction band states. Cole used a WKB analysis of the tunneling barrier to extract quantitative lifetime predictions based on these two competing factors.

Femtosecond results for the image potential electron lifetimes on n-heptane/Ag(111) for the $n = 1, 2, 3$ states (23) are shown in Table 1. Several trends are immediately obvious. First, the $n = 1$ lifetimes increase exponentially in accordance with the tunneling picture. Second, looking down the bare surface column, the lifetimes actually get shorter for $n = 2$, as previously measured and discussed by Schoenlein et al (34). This is due to the fact that $n \geq 2$ are degenerate with the projected bulk conduction band on Ag(111), while $n = 1$ is in the gap. However, the presence of a monolayer reduces the work function and moves the $n = 2$ state into the gap, allowing the dependence of lifetime

Table 1 Comparison of measured lifetimes with values calculated from Cole's model

Quantum number	Bare (fs)	Monolayer (fs)		Bilayer (fs)		Trilayer (fs)	
	Data	Data	Prediction	Data	Prediction	Data	Prediction
$n = 1$	32	155	80	1580	1040	17600	13300
$n = 2$	≤ 20	260	220	500	570	1320	3100
$n = 3$	65	700	670	1000	920		3600

on n to assume the normal dependence. Whether $n = 3$ is still degenerate or whether it is simply substantially decoupled from the metal by the dipole layer induced in the monolayer by contact with the metal is an interesting question (23).

Third, looking across the $n = 2, 3$ rows in the Table 1, it is clear that the increase in lifetime is slower than for $n = 1$. This can be explained by looking at the bilayer model potential shown in Figure 8. The $n = 2, 3$ states are near the top of the barrier and are only weakly influenced by it. This difference in the effect of the tunneling barrier for the various quantum levels is most obvious in looking down the bilayer row: The $n = 1$ lifetime is longer than $n = 2$ or 3. However, the effect of the classical oscillation time in the outer well is manifested by the fact that the $n = 3$ lifetime is longer than $n = 2$, in spite of seeing practically no tunneling barrier at all. Thus this simple model is able to capture the essential physics of tunneling and the classical oscillation time and predict the nonmonotonic trends in lifetime as a function of quantum number for a given layer thickness.

DYNAMICS OF ELECTRONS IN QUANTUM WELLS

The dynamics of electrons in the presence of physisorbed layers of xenon on a metal substrate differ significantly from electron dynamics in the presence of alkane layers, because solid Xe has an attractive electron affinity. In the case of alkane layers, the dynamics are dominated by tunneling through the potential barrier due to the alkane layer, whereas in the case of xenon layers, the dynamics are best described as due to the quantum well (QW) nature of the states. While the dynamics are quite different between the two systems, a modified version of the model used to describe image states outside alkane layers agrees with both the experimental binding energies of the Xe QW states and the dynamics data obtained by time-resolved TPPE. The study of xenon also benefits from the fact that the band structure of solid Xe has been characterized extensively by photoemission (51, 52) and state-of-the-art band structure calculations (53). Such a well-characterized system can serve as a valuable test

for model predictions of energy levels and electron transport at metal-insulator and metal-semiconductor heterojunctions and quantum-confined systems.

Several groups have pioneered the non-time-resolved study of excess electrons in metallic QWs. Himpsel, Willis, and coworkers (54) used inverse photoemission to characterize the development of QW states above the Fermi level for a variety of overlayers such as Cu, Ag, Au, Co, and Fe on various substrates, including Co(100), Fe(100), Cu(100) and Au(100). Smith et al (55) have contributed to the theoretical descriptions of these systems. Au grows on Pd(111) in layer-by-layer fashion (56). For this system, the lower band gap of Au relative to the band gap of Pd(111) results in QW states that have been observed using TPPE (19). Using a 1-D scattering model with Pd(111) and Au(111) band parameters, Fischer & Fauster (19) were able to calculate the increased binding energy of the unoccupied state as a function of layer thickness; this was interpreted as the transition of the clean surface $n = 1$ image state to a QW state of the Au layer.

The work described here builds on other recent work that has demonstrated the singular utility of photoemission in general, and two-photon photoemission in particular, for delivering information important to our understanding of the electronic structure and dynamical processes at heterojunctions and quantum-sized systems. A critical insight in the development of the field of photoemission of layered materials is contained in a paper by Loly & Pendry (57). They proposed the technique of recording photoemission spectra of ultrathin slabs on a layer-by-layer basis as a method for accurate band structure determination. The layer thickness quantizes the electron's momentum perpendicular to the surface, removing the momentum uncertainty that limits the resolution of bulk photoemission, resulting in narrow spectral features corresponding to momentum states defined by the layer thickness and the quantum number of the state. By taking spectra at a range of coverages, the entire band (energy as a function of crystal momentum) can be accurately determined. This analysis has been applied to occupied QWs for Cs/Cu(111) (58), Ag/Cu(111) (59), and Xe on noble metals (60, 61) using UV photoemission spectroscopy.

The theoretical framework needed to analyze QW states according to the theory of Loly & Pendry (57) is developed next. QW wave functions possess a factor of $\sin k_z z$. Wave functions in a layer N atoms deep must vanish at $z = 0$ and Nd , where d is the interplanar spacing, leading to the bound state condition $k_z = \pi j / Nd$, where j is the quantum number of the QW state. In the effective mass approximation the energy levels will follow the dispersion relation $E = E_0 + \hbar^2 k_z^2 / 2m^*$. Thus the electronic energy levels of a QW can be thought of as a discretized band structure. A plot of the energies of the states for a range of thickness versus k_z , yields the perpendicular dispersion. Furthermore, the band structure information obtained by this analysis is complementary to

band structure information obtained by angle-resolved measurements of the parallel dispersion: by performing angle-resolved measurements as well as coverage-resolved measurements, a large area of the 3-D surface corresponding to the conduction band [$E(k_{\parallel}, k_z)$] can be determined.

Quantum Well Electronic Structure for Xe/Ag(111)

The TPPE spectra for one to six layers of xenon on Ag(111) are shown in Figure 9 (24). In order to understand the data, let us consider the two cases of s-like and p-like bands in a solid. An s-like band increases in energy as the crystal momentum increases, corresponding to a positive effective mass, while p-like bands decrease in energy as the crystal momentum increases, corresponding to

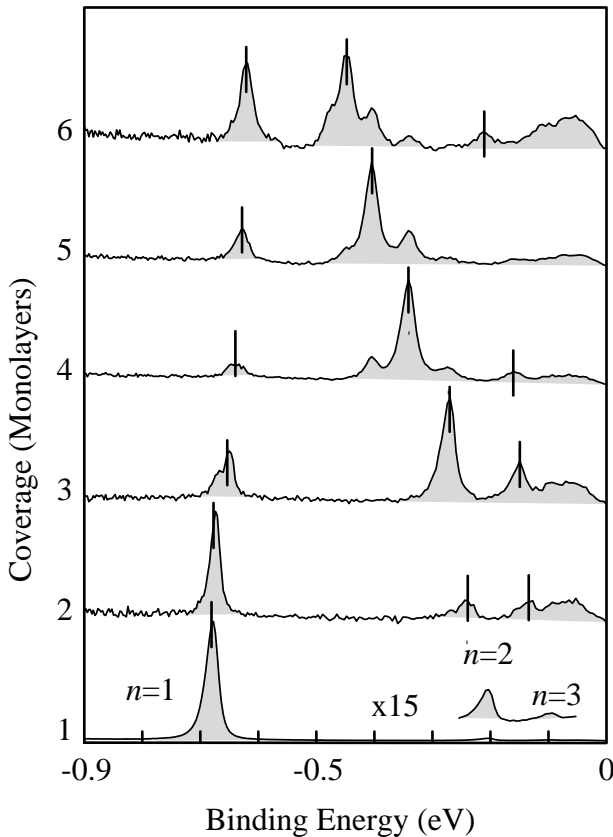


Figure 9 TPPE spectra of Xe/Ag(111) at a series of coverages (one to six atomic layers, approximately). The dark line through the peaks indicates the peak that is assigned to the coverage (in monolayers) indicated at the left of the figure.

a negative effective mass (62). Since the boundary conditions associated with an ultrathin slab limit k_z to large and discrete values associated with the small values of layer thickness Nd , the energy of s-like bands should decrease with increasing layer thickness. The opposite holds for p-like bands. Since the xenon conduction band is derived largely from 6s orbitals, the s-like behavior should be evident in the TPPE spectra of layers of Xe adsorbed on a Ag(111) substrate (Figure 9). The features labeled $n = 2$ and $n = 3$ do indeed decrease in energy (the energy becomes more negative) with the number of atomic layers of Xe adsorbed. The $E(k_z)$ analysis shows that both the $n = 2$ and $n = 3$ states are converging to the bulk Xe conduction band, manifesting the expected QW structure as the electronic structure evolves from 2-D image states towards the 3-D bulk band structure. The result of applying the discrete band structure analysis to the data are shown in Figure 10.

The peak derived from the $n = 1$ state, however, does not show this behavior. The $n = 1$ feature is not, of course, a QW state of some heretofore unknown p-band, but rather owes its existence to the attractive image potential well in the vacuum, which also depends on the number of layers of Xe present on the surface. The complex behavior seen for image states precludes the use of a simple tight-binding or 1-D box model to properly reproduce or explain the coverage dependence. Because of the range of energies involved, i.e. within 1 eV or so of the vacuum level, a successful model must take into account both the image potential well in the vacuum and the band structure of the

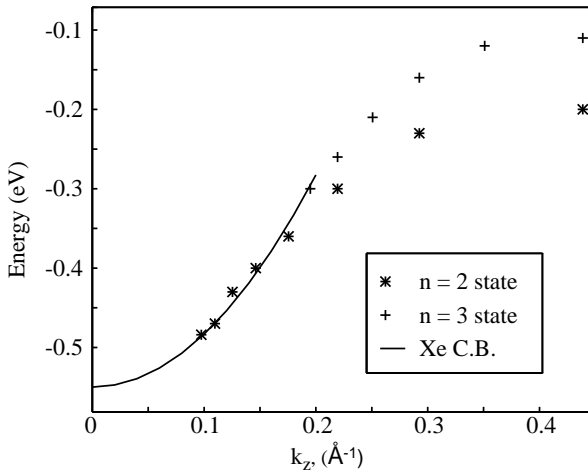


Figure 10 The perpendicular dispersion of the Xe conduction band, from Reference (24), determined by layer-resolved TPPE. The binding energies of the $n = 2, 3$ quantum well states of Xe are plotted as a function of perpendicular momentum.

substrate as well as the conduction band of the adsorbate. McNeill et al (24) have proposed a simple empirical model based on known material parameters that meets these criteria. This model utilizes the two-band NFE model, which has proven successful in reproducing the energies of image states on clean surfaces, and the continuum dielectric model described earlier.

The model uses a piecewise potential consisting of substrate, overlayer, and vacuum potentials. All the constants used are literature values (45, 53, 63), except where noted. In the substrate the two-band NFE approximation (5, 64) is used to describe the wave function in the substrate gap, which has the form of an exponentially damped sine wave with a period of twice the substrate lattice constant. The overlayer is treated in the effective mass approximation using $m^* = 0.55m_e$ (taken from the band structure analysis of the last section, rather than the literature value of $0.35m_e$) and a band (potential) minimum of -0.50 eV with respect to the vacuum level. In the vacuum the potential is taken from the dielectric continuum model for a dielectric constant $\epsilon = 2$. The results of the model are compared to the binding energies for one to nine layers of Xe in Figure 11. The success of the model in reproducing the data leads to the conclusion that models for conduction band QW states must include

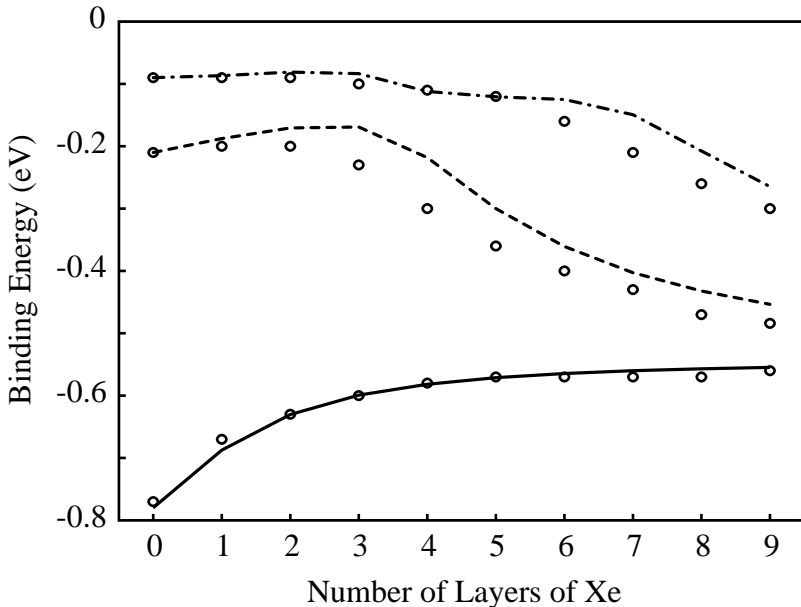


Figure 11 The binding energies of the $n = 1, 2, 3$ quantum well states of Xe/Ag(111) as a function of layer thickness (From Reference 24). Curves are the results of model calculations discussed in the text, where the solid, dashed, and dotted-dashed lines are for $n = 1, 2,$ and 3 , respectively.

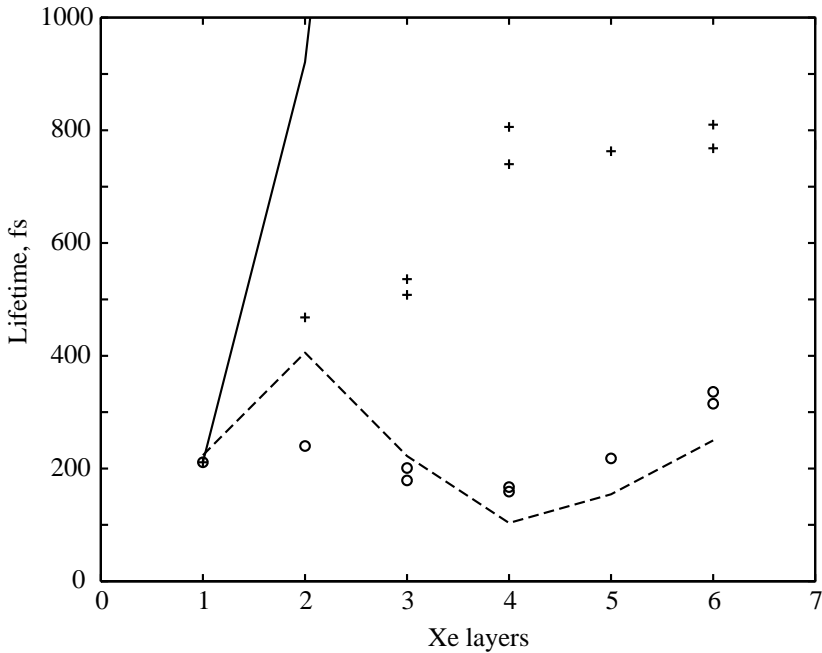


Figure 12 The measured lifetimes of the $n = 1, 2$ states from one to six layers of Xe/Ag(111) along with lifetimes based on the penetration. The $n = 1$ data is represented by + symbols, the $n = 2$ by o symbols. The theoretical lifetimes for the $n = 1, 2$ states are represented by the solid and dashed lines, respectively.

contributions from the substrate and vacuum as well as the overlayer material of interest.

Direct time-resolved studies (25, 26, 65) confirm that the narrow width of the $n = 1$ image state peak for monolayer Xe/Ag(111) (30) is due to longer lifetime. Beyond the monolayer, the lifetimes of the QW states of the Xe layer display a complex dependence on quantum number and coverage (25, 26). The $n = 1$ state lifetime increases monotonically with each additional layer of Xe, while the lifetime of the $n = 2$ state initially increases with the first two layers of Xe, decreases slightly at three layers, then increases again at the fifth and sixth layers (Figure 12).

Lifetime Estimate for Electrons in Quantum Wells

It is reasonable to assume that the primary decay pathway for electrons at the Xe/Ag(111) interface is via electron-vacancy recombination in the substrate. Based on this assumption, the lifetime should primarily depend on the wave function overlap with the substrate. An intuitive and somewhat successful model

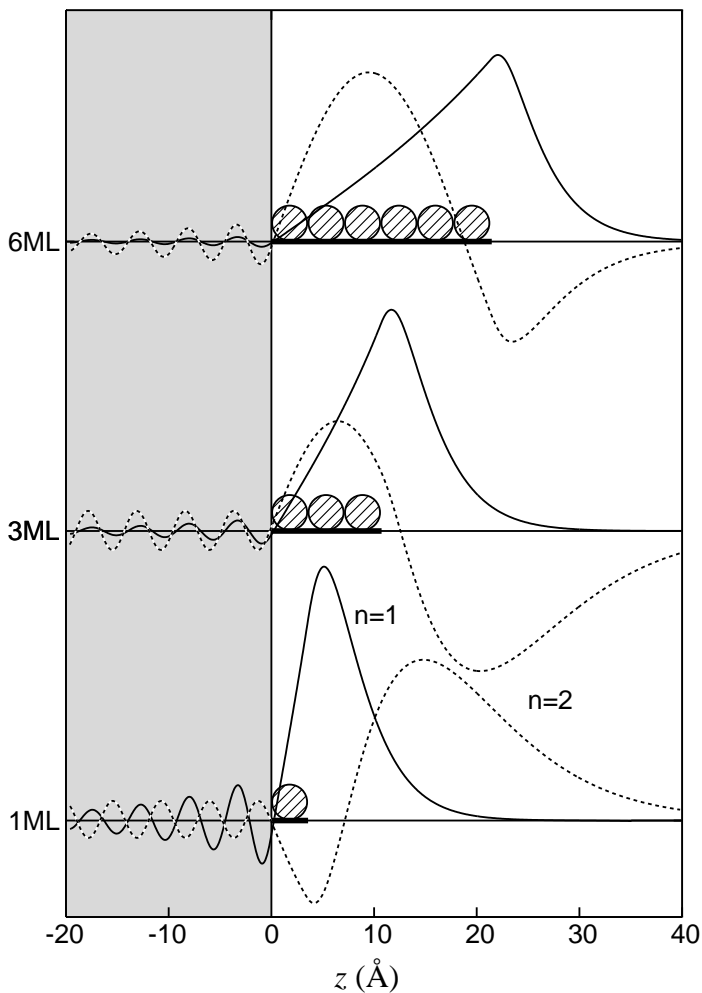


Figure 13 The resulting wave functions for the quantum well model for the $n = 1$ (solid lines) and $n = 2$ (dashed lines) states for 1, 3, and 6 layers of Xe/Ag(111). The maximum of the $n = 1$ wave function remains near the overlayer/vacuum interface at all coverages, consistent with the notion that the $n = 1$ state is not a QW state of the layer, but rather an image state of the Xe/vacuum interface. In contrast, the $n = 2$ state changes from image-like (hydrogenic) to quantum-well-like (maximum probability density inside the layer) at higher coverages.

for the lifetime of image states starts by assuming that the coupling to the crystal is related to the penetration p of the image state into the bulk, where p is defined as the probability density in the bulk (66–69),

$$p = \int_{-\infty}^0 \psi^* \psi dz. \quad 11.$$

The lifetime broadening Γ of the image state is related to the linewidth of the bulk crystal conduction band $\Gamma_b(E)$ by $p \cdot \Gamma_b(E)$. Wolf et al (65) applied this ansatz to account for the lifetimes of $n = 1, 2$ for a monolayer of Xe/Cu(111). Applying this formalism to the wave functions calculated previously, we obtain theoretical lifetimes for the $n = 1$ and $n = 2$ states (Figure 12). The calculated lifetimes agree with the measured lifetimes to within a scaling factor: A phenomenological Γ_b is determined by a fit to the data. Some insight into the trends can be gained by examining the wave functions (Figure 13). The maximum in the $n = 1$ wave function remains near the layer-vacuum interface at thicker coverages and is exponentially damped within the layer, consistent with the long lifetimes observed for the $n = 1$ state. In contrast, the $n = 2$ wave function begins to move inside the layer for three layers, allowing wave function penetration into the substrate to increase. As the QW widens, the probability density begins to move out of the substrate into the QW.

While these results help to form a picture of some of the relevant physics in the dynamics of excited carriers in QWs, many aspects of the dynamics are left out in this simplified quantum-mechanical picture. The possible role of decay within the layer is not explored. The potential used is probably not accurate within an Ångstrom or two of either interface, while the model results are sensitive to the potential in this region. Nevertheless, this constitutes a partial understanding of the complex dynamics of electrons at a metal-dielectric interface, and establishes a general method by which layer-by-layer TPPE can be used to probe interfacial dynamics as a function of layer thickness and perpendicular and parallel carrier momentum.

DYNAMICS OF CARRIER LOCALIZATION AT INTERFACES

The delocalization and localization of electrons in condensed-phase environments is fundamentally interesting, especially at material interfaces where lower dimensionality may result. For example, the interplay between kinetic and potential energies can result in interesting phenomena such as the metal-insulator transition. Electrons in a number of physical systems exhibit two-dimensional behavior (12, 70, 71). The spatial extent and the transport properties of electrons supported on a liquid helium surface have been the subject of extensive

experimental and theoretical studies. Interesting features such as the Coulomb crystallization on bulk helium (72) and the polaronic transition on a helium film (73) were experimentally observed. However, the problem of electron localization at atomically thin insulator-metal interfaces remains poorly understood owing to complexities associated with the morphology of the interface, the electronic structure of the substrate and the overlayer, and the coupling to the vibrational modes of the composite system.

Unlike the core electrons tightly bound to atomic nuclei, valence electrons in metals are normally delocalized to a greater or lesser degree as manifested by how much the bands disperse. One important phenomenon that happens near an interface is that delocalized electrons can become localized in one or more directions (4–8, 74). Image potential electrons are held close to the surface by the image potential but can move relatively freely parallel to it. The motion of the electron along the interface and how it is affected by the substrate and the presence of overlayers can be directly studied by angle-resolved TPPE. Here we review the recent angle-resolved TPPE results for excess electrons on Xe/Ag(111) (24) and alkane/Ag(111) (25, 27, 50). These studies demonstrate the effectiveness of this technique in determining the effective mass of excess electrons at interfaces and show that it can be used as a new probe of electron localization in 2-D systems.

For electrons behaving like free particles along the interface, angle-resolved TPPE data will yield a dispersive band. Electrons are in extended states, and k_{\parallel} is a good quantum number. These delocalized states are characterized by an effective mass, m^* , which can be determined by a fit to the parabolic dispersion, $E = \hbar^2 k_{\parallel}^2 / 2m^* + E_0$. Extensive studies have shown that the image potential electrons on various crystalline bare metal surfaces have effective masses close to that of a free electron (3, 31, 75). On the other hand, spatially localized electrons result in a nondispersive feature in the spectrum. A localized state is a superposition of many k_{\parallel} plane waves; therefore photoelectrons can be ejected over a range of angles. However, the energy is not a function of k_{\parallel} , so angle-resolved TPPE will yield a flat energy band as a function of angle.

At the Kr and Xe/Ag(111) interfaces, an excess electron remains delocalized for all coverages (24). For both the $n = 1$ and $n = 2$ states of Xe overlayers, the effective mass goes from that of a free electron at monolayer coverage ($0.95 \pm 0.1m_e$ for $n = 1$) to significantly less than that of a free electron ($0.6 \pm 0.2m_e$ for $n = 1$) at four layers. The dispersion data for one to two layers of Kr is similar to that of Xe. The decrease of effective mass toward the literature values for the bulk Kr and Xe conduction bands [0.42 and $0.35m_e$, respectively (76)] demonstrates the influence of the overlayer band structure. The low effective mass and electron delocalization at these heavy rare-gas-metal interfaces is consistent with the fact that free-electron conduction with electron mobilities

of typically a few thousand cm^2/V is found in all the heavier condensed rare gases (76). On the contrary, low mobilities and thermally activated hopping transport are observed for electrons in solid and liquid He^4 and in liquid Ne. The conduction electron repels surrounding rare-gas atoms, creating a lattice expansion or a bubble around the electron. This is a well-known example of self-trapping, in which electrons become stabilized by localizing themselves in the potential well as a result of the self-induced lattice distortion. The composite particle, i.e. localized electron plus strong lattice distortion, is called a small polaron and is discussed further below. The occurrence of a bubble is associated with the negative electron affinity in condensed phases of the light rare gases. For these atoms, the short-range pseudopotential is dominated by the strongly repulsive interaction between the excess electron and the atomic core. In heavier rare-gas atoms and molecules the polarizability becomes significant, softening the sharp Pauli repulsion by the core. The interaction between an excess electron and a rare-gas lattice becomes attractive for Kr and Xe.

In angle-resolved TPPE study of various alkanes on the Ag(111) surface, both localized and delocalized states are found (50). Figure 14 shows the angle-resolved TPPE spectra of $n = 1$ image electrons on bilayer neopentane and n-pentane taken with a laser pulse duration of several picoseconds. For n-alkanes and cyclohexane, in addition to the dispersive feature normally expected for the delocalized electrons ($m^* \approx 1.2m_e$), a nondispersive peak is observed and attributed to localized electron states. However, layers of neopentane do not induce a localized state even up to trilayer thicknesses. Based on the non-time-resolved TPPE data, it was proposed that the geometry of adlayer molecules and their resultant low-energy electron scattering properties are linked to the electron localization observed in the 2-D films (50). The results were correlated with excess electron mobility data for nonpolar liquids, since mobility in liquid neopentane is two to three orders of magnitude higher than in n-alkanes or cyclohexane (77). This was the first work to observe localization of excess electrons at an interface as a nondispersive feature in angle-resolved photoemission.

Small Polaron Formation in Two Dimensions

Femtosecond time- and angle-resolved TPPE studies of the alkane-metal system were recently performed to determine the dynamics of the electron localization processes. Based on the results, it was proposed that the mechanism for localization is self-trapping (25, 27). Before going to the results, we briefly discuss some aspects of small polaron theory (76, 78–80). Consider the fate of an excess electron introduced into a deformable lattice. We first assume that the excess electron is localized at a single lattice site without lattice distortion. The electron wavepacket includes Bloch waves throughout the conduction band, with average energy near the band center. This localized electron has a tendency to

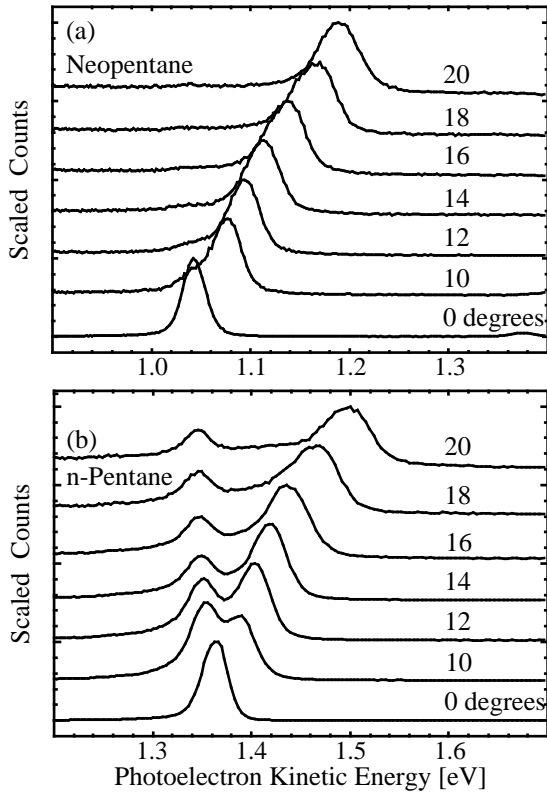


Figure 14 The dispersion of the $n = 1$ image state in the presence of a bilayer of (a) neopentane and (b) n-pentane on Ag(111), from Reference (50). The n-pentane possesses a non-dispersive feature absent in the neopentane dispersion data.

become delocalized by lowering its energy to reside at the bottom of the conduction band. The localization energy, E_{loc} , is the energy expense of keeping the electron localized and can be estimated from the half width of the conduction band according to Gilbert (81). On the other hand, the localized electron could dig itself an attractive potential well by polarizing and displacing the atoms surrounding it. If the energy gain upon lattice relaxation, E_{relax} , exceeds the threshold expense of localization energy, the electron will be self-trapped with a self-trapping energy:

$$E_{st} = E_{relax} - E_{loc} > 0. \quad 12.$$

Thus the degree of localization of carriers in a crystal is determined by a balance of these two opposing tendencies, and the competition between the two is

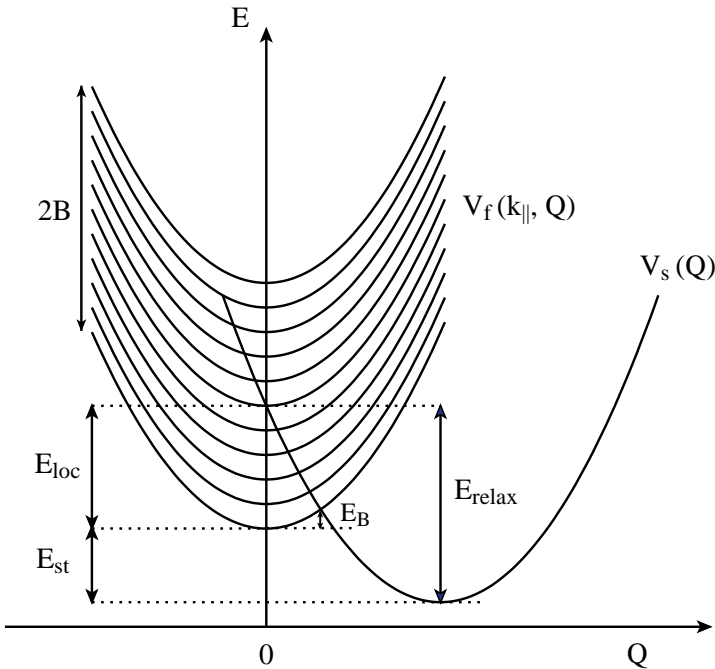


Figure 15 Potentials for the delocalized and localized states as a function of lattice distortion coordinate (Q) are indicated by $V_f(k_{\parallel}, Q)$ and $V_s(Q)$, respectively. Each curve in the V_f manifold represents a different k_{\parallel} state. The band width ($2B$), localization energy (E_{loc}), lattice relaxation energy (E_{relax}), self-trapping energy (E_{st}), and self-trapping barrier (E_B) are depicted. See discussion in text.

shown in Figure 15, where the potentials $V_f(k_{\parallel}, Q)$ and $V_s(Q)$ are associated, respectively, with the free states (without electron-phonon coupling) and the self-trapped state, and Q is the phonon coordinate responsible for self-trapping.

The stability of a polaron depends on the nature and the strength of the coupling between electron and lattice, the dimensionality of the lattice, and other parameters. A clear analysis using an adiabatic approximation and a continuum model was given by Emin & Holstein (82) and Toyozawa and coworkers (83–85). As pointed out by their scaling argument, if only short-range electron-lattice coupling is considered, then in 3-D delocalized and strongly localized states separated by a barrier are always predicted. In 1-D only a localized state is predicted. In contrast, localization in two dimensions is a subtle problem, since there is near-equality of the localizing and delocalizing tendencies. A small change in a physical parameter can easily tip the balance in favor of one

tendency over the other. Thus two dimensionality is often called the marginal case (85–87). This delicate balance seems to manifest itself in the ≤ 10 meV energy gap between the bottom of the parabolic band and the localized state at $k_{\parallel} = 0$ for the $n = 1$ image electrons on alkane/Ag(111) system (Figure 14). This energy separation is independent of layer thickness for one to three layers of alkane and is an indication of the self-trapping energy in this 2-D system.

Let us now consider the dynamical process of self-trapping from delocalized states. As is mentioned above, for the 3-D case a short-range electron-continuum interaction always yields an adiabatic barrier that separates a small polaron state from a free state. For the 2-D case, such a barrier also exists when taking into account the discreteness of the lattice (87, 88). To the lowest-order approximation, the potentials for the free and self-trapped states are shown in Figure 15. For delocalized free states, the energy for electron motion along the surface is defined by a dispersion relation $E_{\parallel}(k_{\parallel})$. Within the harmonic approximation, the energy of the free band upon lattice distortion is quadratic in the phonon coordinate Q and represented by parabolic potential $V_f(k_{\parallel}, Q)$ for various k_{\parallel} values, where the minimum of each parabola at phonon coordinate $Q = 0$ corresponds to the band energy E_{\parallel} for an undistorted lattice. The electron-phonon interaction is considered to be linear in Q . The potential of the self-trapped state is then a displaced parabola V_s with the same curvature as V_f . The point where V_s crosses $V_f(k_{\parallel}, Q)$ represents the potential barrier that must be overcome in order for self-trapping to occur. The barrier height is large at $k_{\parallel} = 0$, decreases with k_{\parallel} until V_s crosses $V_f(k_{\parallel})$ at $Q = 0$, then turns around to increase with k_{\parallel} . Therefore the self-trapping rate will have a dependence on k_{\parallel} . On the other hand, the rate at which the self-trapped electrons form will be an averaged sum over self-trapping rates from all k_{\parallel} values (25, 27).

Femtosecond Dynamics of Polaron Formation at the Interface

Consistent with this picture, the femtosecond results show that there is a time delay between initially populating the image state and the formation of the localized electrons. According to the Franck-Condon principle, optical excitation primarily creates electrons in the free states with no lattice distortion (Figure 16a). The excited electrons can then be stabilized by self-trapping and become localized at a later time (Figure 16b).

Detailed lifetime measurements have been done at various angles to investigate the momentum dependence of the dynamics (25, 27). The rise and decay times extracted from bilayer data are tabulated in Table 2. Within the error of fitting the localized feature exhibits the same 400-fs rise and 1550-fs decay over the range of angles studied. In contrast, the dynamics of the delocalized states have strong momentum dependence. The decay times vary from 810 fs ($k_{\parallel} = 0$) to 200 fs (highest k_{\parallel} observed). This comparison suggests that initially

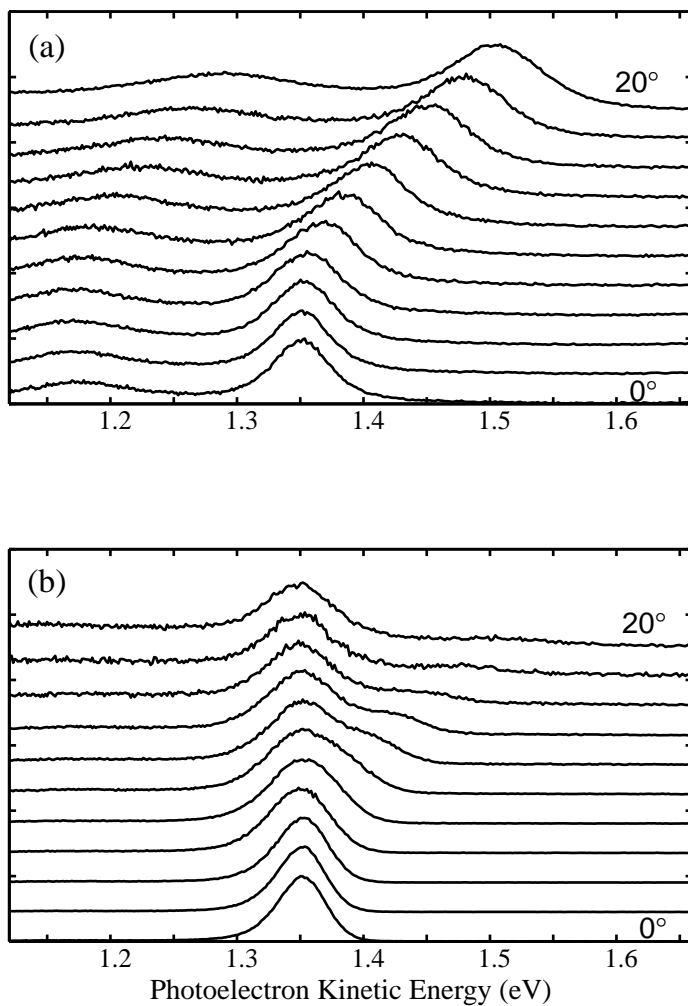


Figure 16 Femtosecond angle-resolved TPPE spectra of $n = 1$ states on bilayer n-heptane/Ag(111) taken at pump-probe delay time of (a) 0 and (b) 1670 fs. Initially the electron is in the delocalized state. Then the electron becomes localized within a few hundred femtoseconds.

Table 2 Rise and decay times for delocalized and localized states on bilayer n-heptane/Ag(111)

Angle (degree)	k_{\parallel} (\AA^{-1})	Delocalized feature		Localized feature	
		Rise (fs)	Decay (fs)	Rise (fs)	Decay (fs)
0	0	780	810	950	1260
4.4	0.05	660	720	740	1490
6.4	0.07	510	550	600	1610
8.4	0.09	380	390	380	1530
10.4	0.12	320	360	350	1570
12.4	0.14	250	330	290	1620
14.4	0.16	160	330	400	1520
16.4	0.18	120	270	340	1630
18.4	0.20	90	230	390	1580
20.4	0.23	70	200	400	1570

delocalized electrons self-trap into the localized state with self-trapping rates depending on their k_{\parallel} values, and that the localized state grows in with a rate averaged over the decay rates of all delocalized states. These self-trapped interfacial electrons are not in the ground state of the system, and their decay is determined by tunneling through the overlayer back into the metal (23).

The k_{\parallel} dependence of the self-trapping rate can be modeled as an activated barrier crossing when the system has a thermal energy higher than the phonon energy (89). Without knowing the coupling strength between the delocalized and self-trapped states, it is hard to determine whether the process of barrier crossing is adiabatic or non-adiabatic. Assuming that the coupling is large enough for adiabatic processes but smaller than $k_B T$, i.e. in the classical adiabatic limit, the self-trapping rate can be described by (90)

$$k_{\text{st}} = \frac{\omega}{2\pi} e^{-E_B/k_B T}, \quad 13.$$

where ω is the phonon frequency associated with the lattice distortion along the phonon coordinate Q in Figure 15. The height of the barrier E_B can be expressed in terms of E_{st} and E_{relax} , and thus

$$\ln k_{\text{st}} = -\frac{[E_{\text{st}} + E_{\parallel} - E_{\text{relax}}]^2}{4E_{\text{relax}}k_B T} + \ln \frac{\omega}{2\pi}. \quad 14.$$

Taking the self-trapping rate to be the difference of the decay rates of the delocalized state and the tunneling rate of the localized state, $\ln k_{\text{st}}$ versus $E_{\text{st}} + E_{\parallel}$ is plotted along with its parabolic fit in Figure 17. The abscissa and ordinate of the vertex of the parabola give $E_{\text{relax}} = 0.16$ eV and $\hbar\omega = 130$ cm⁻¹. This treatment is similar to the well-known Marcus theory for electron transfer (91).

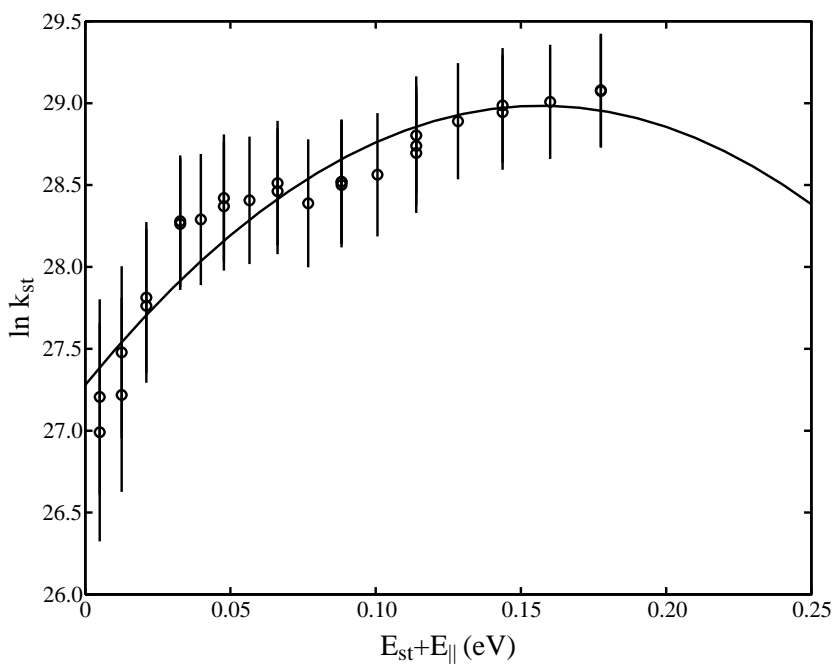


Figure 17 Energy dependence of the self-trapping rates for $n = 1$ states on bilayer n-heptane/Ag(111). The fit to the data yields the lattice relaxation energy and the phonon energy responsible for self-trapping. See discussion in text.

The inverted region is not observed in the data, as a result of the limited angle range accessible by the sample goniometer in the experiment. Nevertheless, such a slow down in self-trapping rate after the energy exceeds a certain value is predicted (92, 93), and presumably would be observed at large angles.

This characteristic phonon energy of 130 cm^{-1} responsible for self-trapping is higher than the acoustic phonon energy of an n-heptane crystal at the Brillouin boundary [$20\text{--}60 \text{ cm}^{-1}$, estimated from the speed of sound (94) and the lattice constant (95)]. It implies that higher frequency modes such as intramolecular vibrations may be involved in small polaron formation. The intramolecular vibrations of n-heptane cover the energy range from 50 to 3000 cm^{-1} (96). Thus, it is reasonable to consider that formation of the small polaron involves both intra- and intermolecular vibrations, i.e. the small polaron is a hybrid of a molecular polaron and a lattice polaron.

The lattice relaxation energy is closely related to the reorganization energy used in electron transfer theory. For polyacene crystals the lattice relaxation energy for formation of a molecular and lattice polaron is on the order of

0.18 eV (97). The interaction energy is expected to be less in the case of a 2-D small polaron, owing to fewer neighbors. Still, the magnitude of E_{relax} from the fit shows the consistency between the data and the small polaron picture.

It is interesting to compare the lattice relaxation energy with the localization energy. The localization energy can be estimated by the half bandwidth, B . Within the isotropic 2-D tight binding approximation, the half bandwidth is related to the effective mass of the band by $B = \frac{2\hbar^2}{m^*a^2}$, where a is the lattice constant. The effective mass of the delocalized state is $1.2 m_e$. The localization energy is estimated to be ≈ 0.25 eV using the n-heptane surface mesh dimensions (95). However, this approach may result in an overestimation (≈ 1.5 times) of the electron kinetic energy of strongly localized states (85). The localization energy is thus comparable to the lattice relaxation energy (≈ 0.16 eV). This explains why the self-trapping energy given by Equation 12 is small for this 2-D system.

CONCLUSIONS

Surface physics and chemistry are areas of great fundamental and practical importance that have developed rapidly over the past several decades. Early theories describing simple surface states split off from the valence band have developed into sophisticated treatments that include image potential states, valence and conduction band QW states, and localized states due to chemical bonding at interfaces. Using femtosecond two-photon photoemission, researchers have elucidated the influence of the substrate bands, overlayer electronic structure, dielectric screening, electron tunneling, and polaron formation on the dynamics of electrons at interfaces. These results are also spurring advances in the theory of electronic structure at interfaces and surface photochemistry.

Probable future developments include the application of TPPE to study complex metal-organic interfaces approximating electronic polymer junctions. Significant advances in the use of femtosecond vacuum UV sources for probing valence and core levels of surface and adsorbate species (98) are likely. Other work currently being undertaken includes spin-selective femtosecond TPPE of magnetic heterostructures. Over the next few years femtosecond photoemission will undoubtedly yield important results on a variety of fundamentally and technologically interesting systems.

ACKNOWLEDGMENTS

This work was supported by the Director, Office of Energy Research, Office of Basic Energy Sciences, Chemical Sciences Division of the U.S. Department of Energy, under Contract No. DE-AC03-76SF00098. The authors acknowledge NSF support for specialized equipment used in some experiments described herein.

Visit the Annual Reviews home page at
<http://www.annurev.org>

Literature Cited

1. Avouris P, Walkup RE. 1989. *Annu. Rev. Phys. Chem.* 40:173–206
2. Haight R. 1983. *Surf. Sci. Rep.* 21:275–325
3. Fauster Th, Steinmann W. 1995. In *Electromagnetic Waves: Recent Developments in Research, Vol. 2: Photonic Probes of Surfaces*. ed. P Halevi, pp. 347–411. Amsterdam: Elsevier
4. Tamm IE. 1932. *Phys. Z. Sowjetanion* 1:733
5. Maue AW. 1935. *Z. Phys.* 94:717
6. Goodwin ET. 1939. *Proc. Cambridge Philos. Soc.* 35:205
7. Goodwin ET. 1939. *Proc. Cambridge Philos. Soc.* 35:221
8. Shockley W. 1939. *Phys. Rev.* 56:317
9. Ashcroft NW, Mermin ND. 1976. *Solid State Physics*, pp. 367–69. New York: Saunders
10. Smythe WR. 1950. *Static and Dynamic Electricity*. New York: McGraw-Hill
11. Landau LD, Lifshitz EM. 1984. *Electrodynamics of Continuous Media*. Oxford: Pergamon
12. Grimes CC, Brown TR. 1974. *Phys. Rev. Lett.* 32:280–83
13. Johnson PD, Smith NV. 1983. *Phys. Rev. B* 27:2527
14. Dose V, Altmann W, Goldmann A, Kolar U, Rogozik J. 1984. *Phys. Rev. Lett.* 52:1919
15. Straub D, Himpfel FJ. 1984. *Phys. Rev. Lett.* 52:1922
16. Giesen K, Hage F, Himpfel F, Riess HJ, Steinmann W. 1985. *Phys. Rev. Lett.* 55:300
17. Fischer R, Schuppler S, Fischer N, Fauster Th, Steinmann W. 1993. *Phys. Rev. Lett.* 70:654
18. Fischer R, Fauster Th, Steinmann W. 1993. *Phys. Rev. B* 48:15496
19. Fischer R, Fauster T. 1995. *Phys. Rev. B* 51:7112–15
20. Wallauer W, Fauster T. 1995. *Surf. Sci.* 333:731–35
21. Padowitz DF, Merry WR, Jordan RE, Harris CB. 1992. *Phys. Rev. Lett.* 69:3583
22. Cole MW. 1971. *Phys. Rev. B* 3:4418
23. Lingle RL Jr, Ge N-H, Jordan RE, McNeill JD, Harris CB. 1996. *Chem. Phys.* 205:191–203; *Chem. Phys.* 208:297–98
24. McNeill JD, Lingle RL Jr, Jordan RE, Padowitz DF, Harris CB. 1996. *J. Chem. Phys.* 105:3883
25. Harris CB, McNeill JD, Ge N-H, Jordan RE, Lingle RL Jr, Wong CM. 1996. *Ultrafast Phenomena X, Proc. Intl. Conf., 10th, Del Coronado*, pp. 445–47. Berlin: Springer-Verlag
26. McNeill JD, Ge N-H, Wong CM, Lingle RL Jr, Harris CB. 1997. *Bull. Am. Phys. Soc.* 42:316
27. Ge N-H, Wong CM, McNeill JD, Lingle RL Jr, Gaffney K, Harris CB. 1997. *Bull. Am. Phys. Soc.* 42:356
28. Frank KH, Yannoulis P, Dudde R, Koch EE. 1988. *J. Chem. Phys.* 89:7569
29. Kevan SD, ed. 1992. *Angle-Resolved Photoemission. Studies in Surface Science and Catalysis; 74*. Amsterdam: Elsevier
30. Merry WR, Jordan RE, Padowitz DF, Harris CB. 1993. *Surf. Sci.* 295:393–401
31. Giesen K, Hage F, Himpfel FJ, Riess HJ, Steinmann W, Smith NV. 1987. *Phys. Rev. B* 35:971–74
32. Schoenlein RW, Fujimoto JG, Eesley GL, Capehart TW. 1988. *Phys. Rev. Lett.* 61:2596
33. Schoenlein RW, Fujimoto JG, Eesley GL, Capehart TW. 1990. *Phys. Rev. B* 41:5436
34. Schoenlein RW, Fujimoto JG, Eesley GL, Capehart TW. 1991. *Phys. Rev. B* 43:4688–98
35. Echenique PM, Pendry JB. 1978. *J. Phys. C* 11:2065
36. Hertel T, Knoesel E, Wolf M, Ertl G. 1996. *Phys. Rev. Lett.* 76:535
37. Fauster Th, Höfer U, Reuß C, Shumay IL, Thomann U, Wallauer W. 1996. *Presented at Phys. Elec. Conf., Boston, MA*
38. Greenham NC, Friend RH. 1995. *Solid State Phys.: Adv. Res. Appl.* 49:69–70
39. Clinton WL. 1977. *Phys. Rev. Lett.* 39:965
40. Madey TE, Yates JT. 1977. *Surf. Sci.* 63:203
41. Miskovic Z, Vukanic J, Madey TE. 1984. *Surf. Sci.* 141:285
42. Lanzillotto A-M, Dresser MJ, Alvey MD, Yates JT Jr. 1987. *Surf. Sci.* 191:15
43. Dixon-Warren S-J, Jensen ET, Polanyi JC. 1991. *Phys. Rev. Lett.* 67:2395
44. Gomer R, Swanson LW. 1963. *J. Chem. Phys.* 38:1613
45. Echenique PM, Pendry JB. 1990. *Prog. Surf. Sci.* 32:111

46. Smith NV. 1988. *Rep. Prog. Phys.* 51:1227
47. Wannier GH. 1943. *Phys. Rev.* 64:358
48. Schuppler S, Fischer N, Fauster Th, Steinmann W. 1990. *Appl. Phys. A* 51:322.
49. Lingle RL Jr, McNeill JD, Jordan RE, Harris CB. 1994. *Presented at Annu. Meet. Am. Chem. Soc., 204th, Washington, DC*
50. Lingle RL Jr, Padowitz DF, Jordan RE, McNeill JD, Harris CB. 1994. *Phys. Rev. Lett.* 72:2243
51. Schwentner N, Skibowski M, Steinmann W. 1973. *Phys. Rev. B* 8:2965
52. Schwentner N, Himpfel FJ, Saile V, Skibowski M, Steinmann W, Koch EE. 1975. *Phys. Rev. Lett.* 34:528
53. Bacalis NC, Papaconstantopoulos DA, Pickett WE. 1988. *Phys. Rev. B* 38:6218
54. Ortega JE, Himpfel FJ, Mankey GJ, Willis RF. 1993. *Phys. Rev. B* 47:1540
55. Smith NV, Brookes NB, Chang Y, Johnson PD. 1994. *Phys. Rev. B* 49:332
56. Jaklevic RC. 1984. *Phys. Rev. B* 30:5494
57. Loly PD, Pendry JB. 1983. *J. Phys. C* 16:423
58. Lindgren SA, Wallden L. 1988. *Phys. Rev. Lett.* 61:2894
59. Mueller MA, Miller T, Chiang T-C. 1990. *Phys. Rev. B* 41:5214
60. Schmitzhuhsch T, Oster K, Radnik J, Wandelt K. 1995. *Phys. Rev. Lett.* 74:2595
61. Paniago R, Matzdorf R, Meister G, Goldmann A. 1995. *Surf. Sci.* 325:336-42
62. Hoffman R. 1988. *Solids and Surfaces: A Chemist's View of Bonding in Extended Structures*. New York: VCH
63. Schwentner N, Koch EE, Jortner J. 1985. *Electronic Excitations in Condensed Rare Gases*. Berlin: Springer-Verlag
64. Smith NV. 1985. *Phys. Rev. B* 32:3549
65. Wolf M, Knoesel E, Hertel T. 1996. *Phys. Rev. B* 54:R5295-98
66. Echenique PM. 1985. *J. Phys. C* 18:L1133
67. Echenique PM, Flores F, Sols F. 1985. *Phys. Rev. Lett.* 55:2348
68. Bausells J, Echenique PM. 1986. *Phys. Rev. B* 33:1471
69. de Andres PL, Echenique PM, Flores F. 1989. *Phys. Rev. B* 39:10356
70. Ando T, Fowler AB, Stern F. 1982. *Rev. Mod. Phys.* 54:437
71. Adams PW, Paalanen MA. 1988. *Phys. Rev. Lett.* 61:451
72. Grimes CC, Adams G. 1979. *Phys. Rev. Lett.* 42:795-98
73. Andrei EY. 1984. *Phys. Rev. Lett.* 52:1449
74. Ortega JE, Himpfel FJ, Haight R, Peale DR. 1994. *Phys. Rev. B* 49:13859
75. Straub D, Himpfel FJ. 1986. *Phys. Rev. B* 33:2256
76. Song KS, Williams RT. 1993. *Self-Trapped Excitons*. Berlin: Springer-Verlag
77. Allen AO. 1976. *NBS Rep. NSRDS-NBS 58*, US Dept. Commerce
78. Shluger AL, Stoneham AM. 1993. *J. Phys.: Condens. Matter* 5:3049
79. Gerlach B, Lowen H. 1991. *Rev. Mod. Phys.* 63:63
80. Fisher AJ, Hayes W, Wallace DS. 1989. *J. Phys.: Condens. Matter* 1:5567
81. Gilbert TL. 1966. *Lect. Notes NATO Summer Sch. in Solid State Phys., Ghent, Belgium*. Unpublished, as referenced in Ref. 76
82. Emin D, Holstein T. 1976. *Phys. Rev. Lett.* 36:323
83. Toyozawa Y. 1974. In *Vacuum Ultraviolet Radiation Physics*, ed. EE Koch, R Haensel, C Kunz. pp. 317-30. Braunschweig: Pergamon-Vieweg
84. Toyozawa Y. 1980. In *Relaxation of Elementary Excitations*, ed. R Kubo, E Hanamura. pp. 3-18. Berlin: Springer-Verlag
85. Ueta M, Kanzaki H, Kobayashi K, Toyozawa Y, Hanamura E. 1986. *Excitonic Processes in Solids*. Berlin: Springer-Verlag
86. Toyozawa Y, Shinozuka Y. 1980. *J. Phys. Soc. Jpn.* 48:472
87. Sumi H. 1995. *Int. Conf. Excitonic Proc. Condensed Matter, Darwin, NT, Australia, 19-22 July 1994. Proc. SPIE-The Int. Soc. Opt. Engin.* 2362:108-19
88. Kabanov VV, Mashtakov OYu. 1993. *JETP* 76:647
89. Ioselevich AS, Rashba EI. 1985. *Sov. Phys. JETP* 61:1110
90. Ulstrup J. 1979. *Charge Transfer Processes in Condensed Media, Lecture Notes in Chemistry*. Vol. 10. Berlin: Springer-Verlag
91. Marcus RA, Sutin N. 1985. *Biochim. Biophys. Acta* 811:265
92. Ioselevich AS, Rashba EI. 1985. *Solid State Commun.* 55:705
93. Ioselevich AS, Rashba EI. 1986. *J. Lumin.* 34:223
94. Wortman A. 1958. *The influence of temperature and pressure on the acoustic velocity in some normal-paraffin hydrocarbons*. MS thesis. Univ. Calif., Berkeley
95. Fирment LE, Somorjai GA. 1978. *J. Chem. Phys.* 69:3940
96. Snyder RG. 1967. *J. Chem. Phys.* 47:1316
97. Silinsh EA, Capek V. 1994. *Organic Molecular Crystals. Interaction, Localization, and Transport Phenomena*. New York: AIP. 402 pp.
98. Haight R. 1996. *Chem. Phys.* 205:231